The BepiColombo Environment Radiation Monitor, BERM

Marco Pinto[1,2] · **Beatriz Sanchez-Cano[3]** · **Richard Moissl[1]** · **Johannes Benkhoff[1]** ·
Carlota Cardoso[2,4] · **Patrícia Gonçalves[2,4]** · **Pedro Assis[2,4]** · **Rami Vainio[5]** ·
Philipp Oleynik[5] · **Arto Lehtolainen[6]** · **Manuel Grande[7]** · **Arlindo Marques[8]**

Abstract

The BepiColombo Environment Radiation Monitor (BERM) on board the European Space
Agency's Mercury Planetary Orbiter (MPO), is designed to measure the radiation environ-
ment encountered by BepiColombo. The instrument measures electrons with energies from
~ 150 keV to ~ 10 MeV, protons with energies from ~ 1.5 MeV to ~ 100 MeV, and heavy
ions with Linear Energy Transfer from 1 to $50 \, \text{MeV} \cdot \text{mg}^{-1} \cdot \text{cm}^2$. BERM is operated continu-
ously, being responsible for monitoring the radiation levels during all phases of the mission,
including the cruise, the planetary flybys of Earth, Venus and Mercury, and the Hermean
environment. In this paper, we describe the scientific objectives, instrument design and cal-
ibration, and the in-flight scientific performance of BERM. Moreover, we provide the first
scientific results obtained by BERM during the BepiColombo flyby of Earth in April 2020,
and after the impact of a solar energetic particle event during the cruise phase in May 2021.
We also discuss the future plans of the instrument including synergies with other instruments
on the BepiColombo and on other missions.

The BepiColombo mission to Mercury
Edited by Johannes Benkhoff, Go Murakami and Ayako Matsuoka

✉ M. Pinto
    mgpinto11@gmail.com

1   European Space Research and Technology Centre, European Space Agency, Noordwijk,
    The Netherlands

2   Laboratório de Instrumentação e Física Experimental de Partículas, Lisbon, Portugal

3   School of Physics and Astronomy, University of Leicester, Leicester, UK

4   Instituto Superior Técnico, University of Lisbon, Lisbon, Portugal

5   Department of Physics and Astronomy, University of Turku, Turku, Finland

6   Department of Physics, University of Helsinki, Helsinki, Finland

7   Institute of Mathematical and Physical Sciences, University of Wales, Aberystwyth, UK

8   EFACEC, SA, Oporto, Portugal

1 Introduction

BepiColombo is the first mission of the European Space Agency (ESA) to the Hermean System. It was launched in 2018 and will enter Mercury's orbit in 2025 after completing a series of nine gravity-assisted flybys: one of Earth in 2020, two of Venus, in 2020 and 2021, and six of Mercury in 2021–2025. BepiColombo is composed of two spacecraft, ESA's Mercury Planetary Orbiter (MPO) (Benkhoff et al. 2021) and the Japan Aerospace Exploration Agency (JAXA)'s Mercury Magnetospheric Orbiter (MMO) (Murakami et al. 2020). The propulsion of both spacecraft is provided by the Mercury Transfer Module (MTM), which will separate from the two orbiters after arriving at Mercury. Moreover, because of the expected extreme temperatures, both spacecraft are protected during the cruise phase by the Magnetospheric Orbiter Sunshield and Interface Structure (MOSIF). ESA's MPO carries the BepiColombo Radiation Monitor (BERM) as part of its housekeeping suite. BERM is designed to measure electrons with energies from ~ 150 keV to ~ 10 MeV, protons with energies from ~ 1.5 MeV to ~ 200 MeV, and heavy ions with a Linear Energy Transfer from 1 to 50 MeV $\cdot$ mg$^{-1}\cdot$ cm^2. BERM is responsible for monitoring radiation levels during all mission phases, and ultimately, for sending warning signals to the spacecraft.

The space environment is populated with highly energetic particles originating mainly from three sources. Solar Energetic Particles (SEPs) are sporadic bursts of protons, electrons, and heavier nuclei – accelerated to the MeV–GeV range. SEPs can either be ejected in association with impulsive flare events (IFEs), or accelerated by coronal mass ejections (CMEs) (e.g. Reames 1999). Galactic Cosmic Rays (GCR) are a homogeneous, nearly isotropic, background flux of highly energetic particles with energies reaching GeV and up to 10^{21} eV. GCRs are originated outside the Solar System and are believed to be accelerated by supernovae in our galaxy. GCRs consist mostly of protons ($\sim 90\%$), but also heavier nuclei, predominantly Helium, all the way up to Iron (Potgeiter et al. 2001). Trapped particles in planetary magnetospheres, constitute another source of highly energetic particles. These are dynamic populations of protons and electrons performing torus orbits around the planets, trapped by their magnetospheres, such as the electron and proton Van Allen radiation belts at Earth (Jun et al. 2019). These particles could be potentially detected at Mercury as found by previous missions such as Mercury Surface, Space ENvironment, GEochemistry and Ranging (MESSENGER), where quasi-trapped energetic electrons in Mercury's Magnetosphere, often unable to complete a full orbit around the planet before being lost, were measured (Slavin et al. 2018). It is expected that BERM will measure and characterize these three types of particles during the cruise and Mercury phases.

In addition, BERM observations will strongly depend on the solar cycle, which lasts ~ 11 years, since solar activity is responsible for transient and long-term variations of the radiation environment. During periods of low solar activity (such as during 2018–2021), GCR fluxes increase as a result of the lower modulation level exerted by the heliosphere to charged particles, and the probability of SEP events decreases, whereas during periods of high solar activity (such as the one expected in ~ 2024–2026 at the time of Mercury orbit insertion), the opposite happens (Honig et al. 2019). It is then reasonable to say that even though BERM is a housekeeping instrument, it will provide valuable scientific data regarding the behavior of highly energetic particles in the innermost part of the Solar System.

There are a few other instruments onboard BepiColombo that will perform complementary observations of the radiation environment. These are the Solar Intensity X-Ray and Particle Spectrometer (SIXS) (Huovelin et al. 2020), the Mercury Gamma-Ray and Neutron Spectrometer (MGNS) onboard MPO (Mitrofanov et al. 2021), and the High-Energy Particle instrument for ion (HEP-ion) onboard MMO (Murakami et al. 2020). In fact, there is

currently a continuous cross-calibration effort between the SIXS and BERM teams, using the Earth flyby measurements of both instruments. BERM can measure higher charged particle energies than the other instruments and will be in continuous operation during the cruise phase. Moreover, BERM will also enhance the scientific potential of other instruments such as the Mercury Imaging X-Ray Spectrometer (MIXS) designed to analyse the fluorescence X-rays generated at the surface regolith after being hit by solar X-rays and charged particles (Bunce et al. 2020). It will also complement magnetic field measurements performed by the MPO and MIO Magnetometers (MPO-MAG, MGF, respectively) (Heyner et al. 2021; Baumjohann et al. 2020) that will inform about particle distributions and space weather events. The Search for Exospheric Refilling and Emitted Neutral Abundances (SERENA) (Orsini et al. 2021) on the MPO and the Mercury Plasma Particle Experiment (MPPE) on-board the MMO (Saito 2021), will also benefit from BERM Measurements.

This paper gives a description of BERM, of its capabilities, and of its scientific objectives. In particular, the scientific objectives for the whole mission, including measurements of the Hermean environment and during the cruise phase, are given in Sect. 2; the instrument description is given in Sect. 3; the calibration of BERM with and modelling with Geant4 (Agostinelli et al. 2003) in Sect. 4; the response function of BERM in Sect. 5; flight observations of the Earth radiation belts and a solar energetic particle event are shown in Sect. 6; and finally, the conclusions of this work are given in Sect. 7.

2 Scientific Objectives

The main science objectives of BERM are devoted to the investigation of the radiation environment of Mercury. These objectives are:

1. Characterising the Hermean radiation environment.
2. Investigating the trapped and/or quasi-trapped particles in the Hermean magnetosphere.
3. Characterising the properties of SEPs close to the Sun.
4. Studying the impact of space weather at Mercury, namely the effects of energetic particle bombardment (SEPs and GCRs) in the magnetosphere, exosphere, and surface.

BERM will contribute to the understanding of the Hermean radiation environment, and of solar energetic particles interactions with the magnetosphere of Mercury and its surface together with other instruments such as SIXS and MIXS. It is expected that the instrument will remain in operation all the time during the nominal mission, except when it becomes technically necessary to switch it off. Moreover, multipoint observations of solar energetic particles at different regions of the Hermean system are expected between BERM in MPO and the Solar Particle Monitor (SPM) onboard MMO, a complementary radiation monitor. Even though Mercury is the primary target of BepiColombo, the long trip to Mercury ($\sim$ 7 years) constitutes an exceptional opportunity for heliophysics science, as well as to investigate the sensitivity and performance of BERM in space before its arrival at Mercury. This is true since BERM is almost always in operation during the cruise phase. From launch until 26th May 2021, the instrument was only disconnected during electric propulsion maneuvers for safety reasons. The intervals of these maneuvers are represented in Fig. 7 of Montagnon et al. (2021). From 26th of May 2021 until the end of the mission, it was decided that will be always in operation except when it becomes technically necessary to switch it off. The main reason is to use BERM as a radiation sentinel to issue alarms to switch off other instruments and mitigate their degradation. Consequently, BERM has been recording different energetic particle fluxes encountered by BepiColombo since launch, covering heliocentric

distances of ~ 1.2–~ 0.3 AU. The cruise phase is, therefore, a great opportunity to perform several investigations of the space radiation environment in the inner Solar System and during different periods of solar activity. The main objectives for the cruise phase are:

1. Investigating the planetary radiation environments during the flybys of Earth, Venus, and Mercury.
2. Investigating the propagation of solar particle events.
3. Investigating the properties of Forbush Decreases (large and sudden reductions in the GCR flux) and their potential use as CME tracers (Forbush 1938).
4. Characterizing temporal and spatial variations of GCR fluxes during an extended part of the solar cycle and at heliocentric distances below 1 AU.

3 Technical Overview

3.1 Physical Concept

The BepiColombo Environment Radiation Monitor (BERM) is a 2.143 kg, $174.8 \times 120.0 \times 107.0$ mm^3, energetic charged particle detector based on silicon stack detector technology previously used in the MultiFunctional Spectrometer (MFS), which flew aboard the Alphasat in geostationary orbit from October 2013 to April 2019 (Arruda et al. 2017), and the RADiation hard Electron Monitor (RADEM) that will fly in the future JUpiter ICy moons Explorer (JUICE) scheduled for launch in 2023 (Pinto et al. 2020; Grasset et al. 2013). It consists of a single telescope stack with 11 Fully Depleted, Passivated Implanted Planar Silicon detectors (applied bias of 55–60 V), interleaved by aluminum and tantalum absorbers with an entrance field-of-view of $\sim 40°$. A side-view of the stack is shown in Fig. 2. Detectors are labeled from D1 (detector closer to the telescope entrance) to D11 (detector further away from the telescope entrance). A 25 µm beryllium window is located at the top of the stack, in the middle of the collimator, to cut off low energy electrons (< 50 keV) and protons (< 1.35 MeV). Electrons with energies above 40 MeV and protons with energies above 100 MeV are able to travel through the whole detector stack. The detector is capable of measuring electrons with energies between ~ 0.15–10 MeV, protons with energies between ~ 1.5 and 100 MeV, and Heavy Ions with Linear Energy Transfer (LET) from 1–50 MeV $\cdot$ mg$^{-1} \cdot$ cm^2 (Heavy Ions cannot be distinguished by BERM which means that LET is a more accurate way to describe its measurements). The energy values for electrons and proton detection are higher than the energy cutoff because the minimum energy required for the detector is higher than 100 keV. The physical dimensions of the detectors are given in Fig. 2. The resulting geometric factor, calculated taking into account the whole collimator structure according to (Sullivan 1971), is of 5.5E−04 cm^2 sr. The BERM instrument is mounted in the radiator panel of BepiColombo facing the -Y direction as shown in Fig. 1 (Fuente et al. 2016; Mangano et al. 2021). During the cruise phase it is generally pointing anti-sunward, and during the orbit it will be pointing away from the Sun and from Mercury to also avoid albedo from the planet. We note that the FOV is not blocked by the radiator.

Because of the limited downlink bandwidth, particle events are processed in-flight before the collected data is sent to Earth. Detected particles are assigned to 18 bins, five corresponding to electrons, eight to protons, and five to heavy ions. Two additional bins corresponding to unidentified particles, and to vetoed events (for example particles interacting only with the detector at the bottom of the stack) also exist. The species and energy of a particle passing through the stack is determined by the signal profile (see Sect. 3.2 for more details).
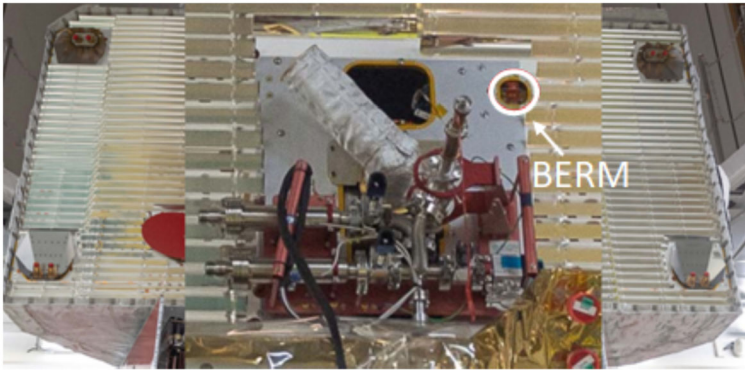
Fig. 1 Location of BERM (white circle) in the radiator panel (-Y) of BepiColombo
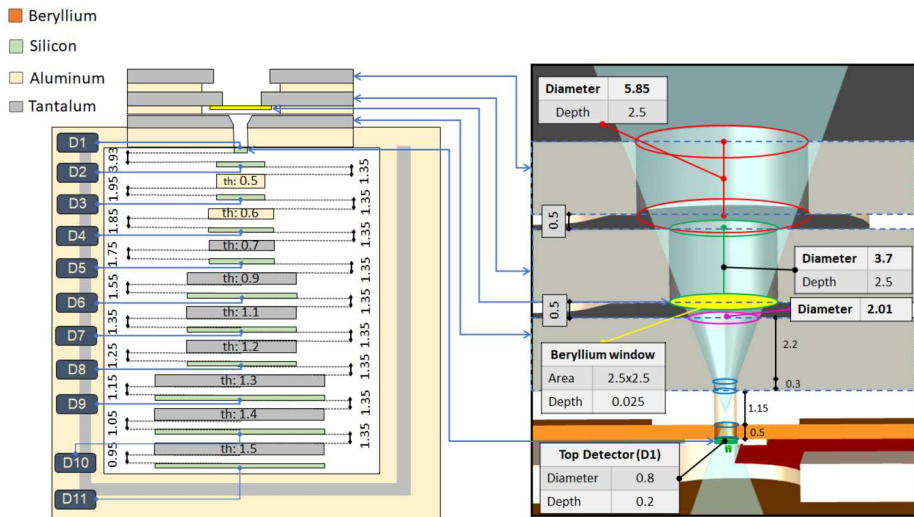

Fig. 2 Side view of the BERM physical concept with the 11 silicon detectors, the tantalum collimator and the side and bottom shielding (left). Top view of BERM's collimator (right). All units are in millimeters. D1 corresponds to the first detector, D2 to the second etc.

3.2 Signal Processing

Energetic charged particles interactions with matter are described by the Bethe-Bloch equation. Higher energy particles lose energy at lower rates than lower energy ones. This means that particles deposit more energy on the detectors at the end of their track. The rate of energy loss is also proportional to the square of the charge of the particle which means that heavy ions lose energy at higher rates than protons allowing to distinguish between these particles. Electrons with energies between ~ 0.15–~ 10 MeV (measured by BERM) are minimum ionizing particles (MIP) which means that they lose energy at lower rates than protons with energies below ~ 100 MeV. Furthermore, as protons travel through the stack losing energy, their energy loss rate increases faster than for electrons which means they can be distinguished by the total deposited energy at the end of their track. For higher energy
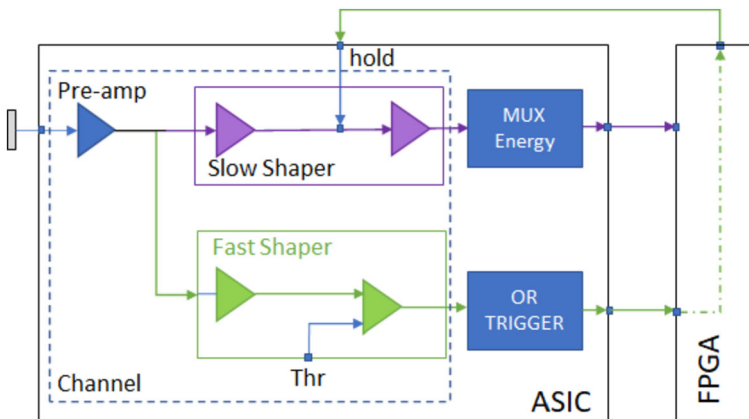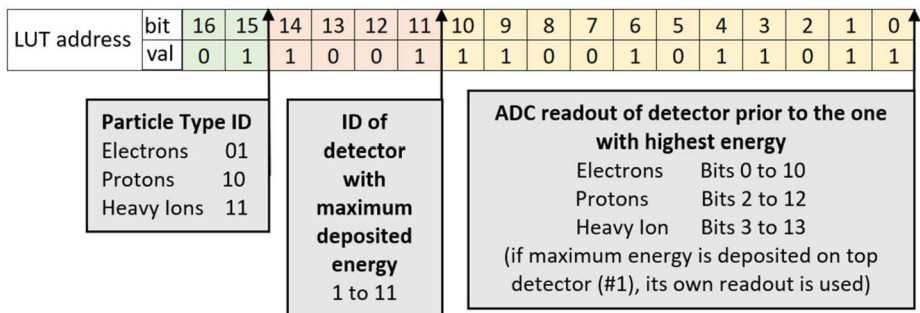
Fig. 3 BERM signal processing. The detector signal processing is performed by IDEAS' VA32TA2_2 ASIC. Each detector is connected to one of the 32 ASIC channels. The ASIC channels follow the VATA logic with a fast shaper for triggering events (in the case of BERM only the channel connected to the top detector is used), and a slow shaper for spectroscopy. Both shaper outputs are read by and FPGA which is responsible for processing all the data before sending it to the spacecraft

protons that can go through the whole detector stack, this does not happen which makes them hard to distinguish from electrons. BERM measures the deposited energy in each of its 11 silicon detectors to discriminate between electrons, protons, and heavy ions. Using this method, it is also capable of determining how far a particle traveled in the stack, and therefore its energy.

The signal generated by particles stopping in BERM's silicon detectors is read by a dedicated VA32TA2_2 Application Specific Integrated Circuit (ASIC) developed by IDEAS depicted in Fig. 3 (datasheet obtained per request from www.ideas.no). Each detector is connected to one of the 32 ASIC channels, each consisting of a pre-amplifier, and a slow and fast shaper unit. The ASIC can handle an input charge from 0 fC to 500 fC (both polarities). The fast shapers of each channel are followed by programmable level discriminators and connected onto a common OR trigger output. In flight, only BERM's top detector (D1 in Fig. 2) is used for the trigger. The discriminator level is in default state (see Sect. 4). The slow shapers integrate the signal for up to 2 μs with a discharge time of ~ 10 μs. The values are then read via an analogue multiplexer after an external signal is applied to the hold unit. This is done by the on-board FPGA's (Field-Programmable Gate Array) that collects the trigger signal and then activates the hold unit before reading the ASIC analogue results for each ASIC channel. The amplitude of the signal for each detector is read into a 14-bit Analogue-to-Digital Converter (ADC) with zero corresponding to the maximum value. Therefore, the values must be inverted. Also, the value of the noise pedestal ($ADC^{PEDESTAL}$), measured during the calibration campaign, must be subtracted to get the true signal amplitude. Since the area of BERM's detectors ranges from 0.5 to 900 mm^2, they have different capacitances (see Table 1), which means that the signal amplitude will reach its peak at different times for each of the detectors. The capacitance between the detectors and the ASIC is of 1 nF. Consequently, the value read from the ASIC is lower for the larger detectors. To correct for this effect, a programmable weight factor is defined for each detector and applied to the amplitude of the signal. The flight (factory) values for the pedestal and the weight factor can be found in Table 1. The values are configurable via a LUT (Look Up Table) that can be updated in future calibration revisions and as a function of equipment aging.

Table 1 BERM detector properties and signal processing default values

Detector #	1	2	3	4	5	6	7	8	9	10	11
Radius (mm)	0.4	4		6.9		11.95			16.95		
Intrinsic Capacitance (pF)	0.4	29		78		189			364		
Thickness (mm)	0.2	0.3									
ADC^{PEDESTAL}	1504	1575	1598	1473	1399	1498	1606	1456	1398	1551	1543
Weight Factor	1					1.2			1.4	1.6	1.8
ADC^{VETO}	8					12			32		NA

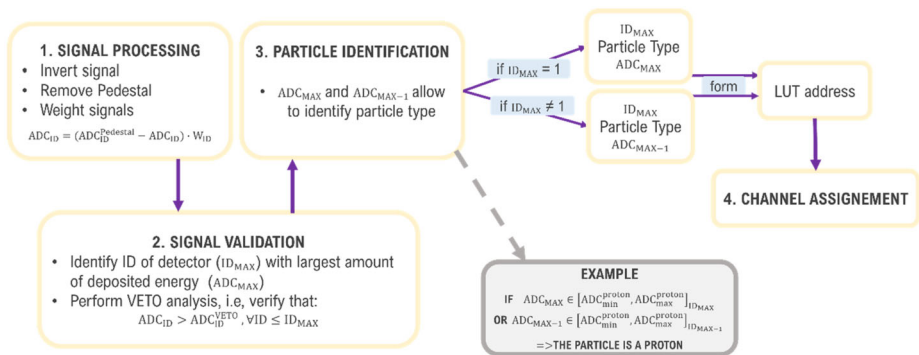**Fig. 4** Energy reconstruction LUT address schematic

The first step of the detection algorithm is to find the detector (ID_{MAX}) where the largest amount of energy was deposited (ADC_{MAX}). After that, a veto analysis is performed to confirm that the event was trigger by a particle passing through all the detectors until ID_{MAX}. Each detector has a minimum ADC^{VETO} value above which is considered to have been originated by the passing of a particle, and under which it should be disregarded and assumed to be noise. The veto analysis consists of checking whether the deposited energy (in ADC) in the detectors preceding ID_{MAX} is greater than their veto values, which are stored in the LUT (see Table 1).

To determine the particle type, the FPGA compares the largest signal, ADC_{MAX}, and the signal from the previous detector, ADC_{MAX-1}, with threshold values that correspond to the minimum and maximum energies that an electron, a proton, and a heavy ion can deposit in those detectors (minimum for electrons is ADC^{VETO}, the maximum for heavy ions is infinite). The intervals defined by these thresholds have no intersection and the particle is identified by determining in which corresponding interval – electron, proton, or heavy ion – the signals can be placed. Once the incident particle is identified, the system will assign it to a determined bin. This is accomplished by creating a 17-bit address containing information regarding the particle type, the detector with larger deposited energy and a selection of 11 bits of the signal measured in the detector that precedes it (see Fig. 4). This address is then searched in the LUT that will associate a bin to the event. For information, Table 2 shows the relation between the different bins and the detector where the maximum amount of energy is deposited.

A full description of event reconstruction from signal processing to particle identification and channel assignment is shown in Fig. 5. Remember that while the algorithm cannot

Table 2 Channels that can be attributed to an event depending on the detector in with the maximum deposited energy

Max. energy deposited on:	1	2	3	4	5	6	7	8	9	10	11	12	13	14	15	16	17	18
	E1	E2	E3	E4	E5	P1	P2	P3	P4	P5	P6	P7	P8	HI1	HI2	HI3	HI4	HI5
D1	X	X				X								X				
D2			X			X	X							X				
D3			X					X							X			
D4				X					X						X			
D5				X							X					X		
D6					X						X					X		
D7					X							X					X	
D8					X							X					X	
D9													X					X
D10													X					X
D11													X					X

Fig. 5 Representation of signal processing (step 1) and recognition algorithm (steps 2–4) of a detected event

be changed, several configuration parameters can be tuned to improve the response of the instrument and/or to account for the aging to its parts.

4 Calibration/BERM Geant4 Model

To characterize BERM's response to radiation, and to optimize its performance, an extensive test campaign was performed at the Paul Scherrer Institute (PSI), Switzerland, in 2014. The tests included pedestal/background measurements, hold-time analysis, count rate linearity, and energy calibration. For this purpose, proton beams from the Proton Irradiation Facility (PIF) with energies ranging from 10 to 200 MeV were used to determine the best readout configuration. The different energies were obtained from two initial proton beam energies,
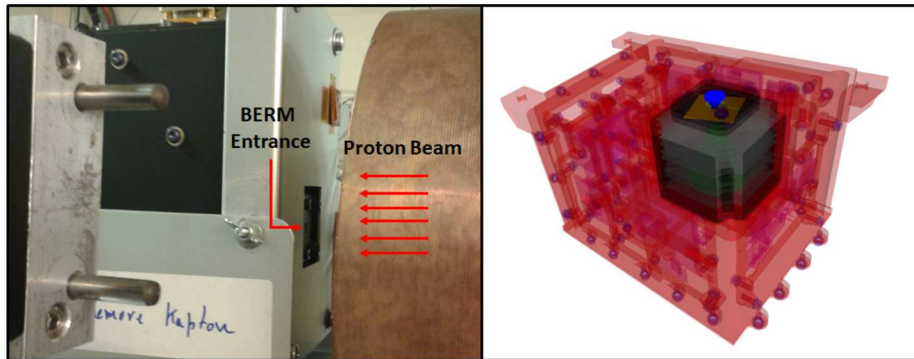
Fig. 6 Proton beam test setup (left), and the Geant4 model used in this analysis with the beam source in blue (modelled after the experimental proton beam characteristics), and the BERM full structure including the aluminum walls in red, screws in gray, silicon detectors in green, tantalum collimator in dark gray, and beryllium window in yellow (right)

73.5 MeV and 230 MeV using copper absorbers to decrease the beam energy. Figure 6 (left) depicts the test setup at PIF.

While the results of these tests were analysed during BERM's development to define the flight configuration, here we revisit the data to obtain the energy-to-ADC coefficients, and to develop a Geant4 (GEometry ANd Tracking) model of the instrument – Geant4 is one of the most widely used particle transport toolkits (Agostinelli et al. 2003). For this purpose, a detailed mechanical model of the instrument (see the right side of Fig. 6) was integrated in the simulations by converting a STEP (Standard for The Exchange of Product Data) file to Geometry Description Markup Language (GDML), via GUIMesh (Pinto and Gonçalves 2019). Simulations were done for each initial proton energy listed in Table 3 using a 40 mm diameter circular source. The energy straggling and angular dispersion values were derived for each energy from first principles calculations.

To validate the BERM Geant4 model, and to compute the response functions of BERM, the energy-to-ADC coefficients were obtained by comparing the Landau-peaks of the deposited energy for different proton energies with the beam test results. Both fast shaper (trigger) and slow shaper (spectroscopy) coefficients should be obtained. However, no dedicated calibration of the fast shaper was performed. A battery of tests will be performed to the Engineering Qualification Model (EQM) using radiation sources, and to the Flight instrument using the Earth flyby measurements to validate the fast shaper (trigger). These will also be used to validate the slow shaper calibration, and the response functions shown in Sect. 5.

4.1 Energy Calibration

To calibrate BERM, i.e., to obtain the energy-to-ADC conversion coefficients, the spectra measured by the detectors for different proton energies was compared to Geant4 simulations (see Table 3). While the spectra at the simulation level are populated only by particle interactions, experimental data has other contributions that need to be considered: electronic noise, crosstalk between the detectors, and pile-up. Noise and crosstalk are associated with the detectors and with the readout electronics. As it can be seen in Fig. 7, particle events interacting in detector #5 and detector #6 have a different profile from the signal induced by noise and cross talk. To remove them from the analysis, the linear relation between each

Table 3 Proton energy scan beam characteristics

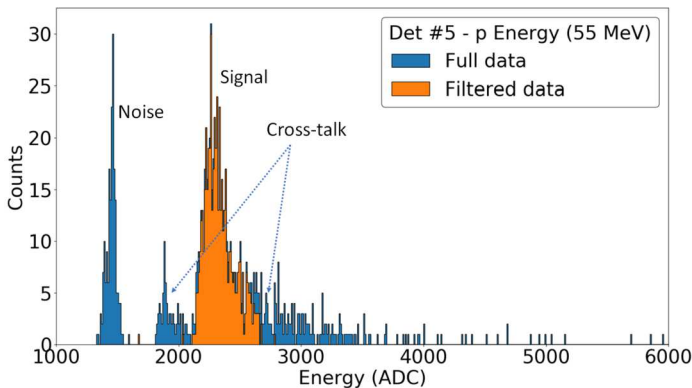| Proton energy (MeV)	Initial energy (MeV)	Flux (p/cm^2/s)	Fluence (p/cm^2)	Cu thickness (g/cm^2)	Energy straggling (MeV)	Angular dispersion (°)
200	230	5.83E+04	1.09E+07	10.30	1.41	0.02
176	230	4.69E+04	1.09E+07	17.92	1.84	4.05
151.2	230	3.69E+04	7.35E+06	25.09	2.15	4.86
139.5	230	3.05E+04	6.29E+06	28.22	2.27	5.17
115	230	2.46E+04	5.16E+06	34.05	2.46	5.72
101	230	2.17E+04	4.19E+06	37.09	2.55	5.99
85.4	230	1.64E+04	3.18E+06	40.32	2.63	6.27
73.5	73.5	1.68E+03	3.79E+05	0.00	0.00	2.00
70.8	73.5	1.53E+03	2.85E+05	0.45	0.28	3.77
55.6	73.5	9.94E+02	1.82E+05	2.69	0.67	7.31
40.7	73.5	6.22E+02	1.16E+05	4.48	0.86	0.61
25.9	73.5	3.93E+02	7.59E+04	5.82	0.97	11.05
19.2	73.5	3.10E+02	6.05E+04	6.27	1.00	11.51
10	73.5	1.99E+02	3.84E+04	6.72	1.03	11.94

Fig. 7 Detector #5 vs Detector #6 spectra computed with Geant4 simulation of a 55 MeV proton beam (left). Detector #5 vs Detector #6 spectra measured by BERM when subject to a 55 MeV proton beam (right). The electronic noise and crosstalk contributions correspond to signals that are not included in the simulations and that can be discriminated

pair of adjacent detectors (#1 and #2, 2# and #3, etc.) associated with crosstalk was calculated. Registries that fell within a small margin of this line and outside the noise area were considered crosstalk. To remove the noise, data from runs with the beam off were used to model the region of interest using a Gaussian fit (see Table 4). Signals within that region were removed in all subsequent analysis. Figure 8 shows the resulting spectra for detector #5. As it can be seen, the method successfully excludes the noise and the crosstalk.

Pile-up is difficult to decouple from the original signal. Pile-up was observed to cause lower signal readouts including shifts in the noise distribution. Using the procedure described in the flux linearity tests (see Sect. 4.2) and considering the observed noise distribution, pileup was found in detectors #2 to #7 for proton energies of 101 MeV and above. For detectors #8 and #9 pileup was found for proton energies of 115 MeV and above, and for

Table 4 Energy-to-ADC coefficients and noise Gaussian parameters for all BERM detectors

Detector #	Energy-to-ADC coefficient (ADC/MeV)	Noise pedestal	
		Mean (ADC)	Std (keV)
1	836.28	1491.05	14.65
2	1098.10	1560.84	12.91
3	1198.30	1588.00	12.04
4	1136.20	1502.00	17.77
5	1204.80	1395.00	25.81
6	975.31	1510.63	65.17
7	958.49	1600.91	86.88
8	931.27	1442.39	96.12
9	826.31	1409.72	163.92
10	807.05	1543.63	171.99
11	855.06	1521.72	95.19

Fig. 8 55 MeV proton beam spectra measured by detector #5 with and without the noise and crosstalk filter

detector #10 and #11 it is observed for proton energies of 139 MeV and above. Beam runs with pileup were not used for the energy calibration.

The calibration curve for each detector was obtained comparing the spectra peak from the beam tests with Geant4 simulations. A Landau function was used to fit both experimental and simulated distributions. Only 70% of the area around the peaks were used since the tail is not fully described by the Landau distribution. The maxima of the experimental and simulated fits were compared for each energy except for 10 MeV protons for which statistical significance was low. Figure 9 shows the results for the top detector (D1). As discussed in Sect. 3, higher deposited energy corresponds to lower proton energies and vice-versa. For high deposited energies (low proton energies) a linear relation is observed between simulated and experimental values. For lower deposited energies (proton energies > 100 MeV), the peak detected by the instrument remains around 1690 ADC while in the simulations the value decreases with increasing proton energy. Simulation results are in accordance with first principles calculations using the stopping power of protons in silicon from the National Institute for Standards and Technology (NIST). Furthermore, the ratio between count rate and the beam flux decreases for higher energies. From the data it is not possible to under-
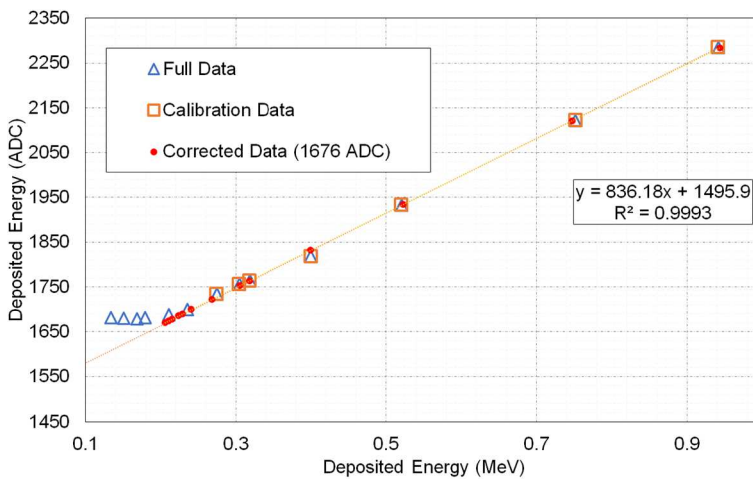
Fig. 9 Calibration curve for the top detector (#1). Full data in blue shows good linearity between the deposited energy from the beam tests and from the simulation for deposited energies above ∼ 0.25 MeV. These values (orange) were used to determine the energy-to-ADC coefficients. In red, it can be seen the data with a Gaussian threshold centered in 1676 ADC
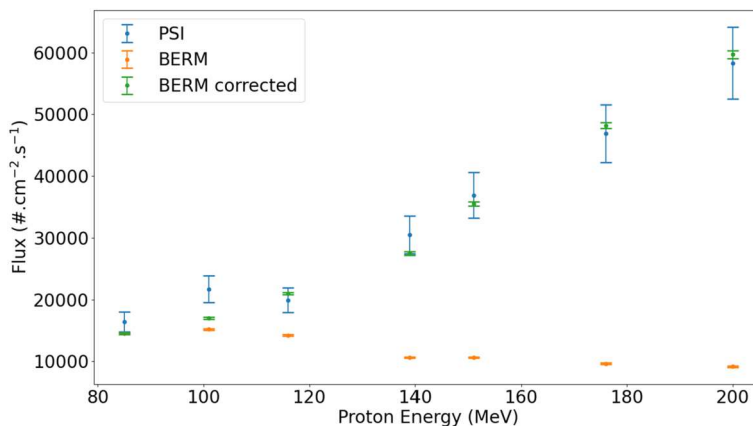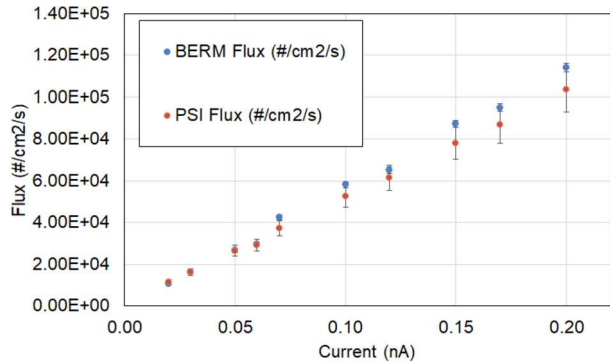

Fig. 10 Comparison between the flux measured by the facilities (PSI blue), by BERM (orange), and by BERM after applying a correction for the efficiency at each energy (green). It is evident from this figure that the high trigger threshold must be taken into account to obtain a reliable measurement of the flux. A 10% error was assumed for the PSI measured fluxes

stand if this is the result of the trigger threshold lying between 1600 and 1700 ADC, or a pile-up effect from the adjacent ASIC channels. Considering the threshold hypothesis, several cutoff values between 1600 and 1700 ADC following a Gaussian distribution with a standard deviation between 0 and 25 ADC, obtained from the pedestal runs, were applied in the simulations using the energy-to ADC conversion coefficient calculated with data from proton energies below 85 MeV for which this effect is expected to be small. A threshold value of 1676 ADC corresponding to ∼ 0.220 MeV with a standard deviation of 20 ADC (24 keV) was found to minimize the differences between experimental and simulated values (see Fig. 9). In Fig. 10, the beam flux measured by BERM was compared to the values pro-

Fig. 11 Comparison between the flux measured by BERM (after correcting for the trigger efficiency) and the flux recorded at the PSI facilities for 200 MeV protons. BERM overestimates the flux by about 10%. This may be related to the uncertainty of the trigger value or other systematic such as the alignment between BERM and the beam

vided by the facility (PSI). As it can be seen, if the efficiency of the trigger is not applied, the flux is underestimated – up to a factor of 6.53 for 200 MeV protons. The larger flux deviation was found for lower proton energies where the trigger has less effect. In these cases, the differences were attributed mainly to systematic errors in the characterization of the beam profile since the whole beam structure, including the copper degraders and collimator were not included in the simulations (although their effect was accounted for in the beam profile at the simulation level as per first principles). For the other detectors no issues were found. Given that the mechanism behind this phenomenon still needs to be verified, a cutoff of 1676 ADC will be considered for the rest of the paper given that no registries below this value are measured in the top detector. The energy-to-ADC conversion coefficients as well as the Gaussian parameters used to fit the noise for each detector can be found in Table 4. In the future, to improve the estimation of the threshold, we will perform radiation tests to the Engineering Qualification Model (EQM) and analyse flight data.

4.2 Flux Linearity – Pile-up

To study the maximum counting rate of BERM, a flux scan was performed. These tests were done with 200 MeV proton beams with fluxes from 1.16×10^4 p/cm^2/s to 1.05×10^5 p/cm^2/s with only the first detector used as a trigger. Figure 11 shows the relation between the flux measured by BERM (corrected for trigger efficiency), and the flux measured by the facility. BERM responded linearly to the increase in flux. BERM overestimated the flux by $\sim 9\%$. This was attributed to two factors: the uncertainty in the threshold (discussed in Sect. 4.1), and to systematic effects such as the alignment between BERM and the beam.

For detectors #2–11, pileup was observed. While this effect is not present in detector #1, Geant4 simulations shows that the particle arrival rate at the top detector for 200 MeV protons is smaller by 2–5 orders of magnitude when compared with the other detectors. This is because 200 MeV protons can go through the whole collimator structure and reach the detectors from outside the FOV opening, i.e., without depositing energy in the first detector. While these particles do not necessary trigger the detector, they add to the signal amplitude of triggered events. This means that, for the higher initial flux the particle arrival rate at detector #2 is in the order of $\sim 5.21 \times 10^4$ particles per second. Since the discharge time of the slow shaper is 10 μs, the theoretical limit is $\sim 1 \times 10^5$ particles per second resulting in pile-up which can affect the whole instrument readout. In fact, this effect is both expected (6.7% probability of having two events in a 10 μs time interval at the highest flux in the second detector) and observed for all tests performed with proton energies above 100 MeV for the second detector.

5 Response Functions

Having successfully modelled the calibration results with BERM's Geant4 model, a new set of Geant4 simulations with the instrument in vacuum were performed. Proton and electron rectangular planar sources with 120×123 mm^2 area and angular isotropic distribution were separated into several energy ranges. An inverse power law energy spectrum was used and renormalized to a flat energy spectrum to optimize the computation time. At analysis level, the deposited energy in each detector for individual events was multiplied by the energy-to-ADC coefficient. Random noise values were generated for each detector according to the corresponding Gaussian distribution obtained in the tests (see Table 4). The trigger threshold described in the previous section was also applied. The final values for the deposited energy were then used as input in the flight algorithm described in Sect. 3. Although there are 18 particle bins, here we analyze only the first 13 corresponding to electrons (bins 1–5) and to protons (bins 6–13). Bins 14–18 corresponding to heavy ions will be studied in a future work. Bins 1–5 are named Electron Bins 1–5 and Bins 6–13 are named Proton Bins 1–8. Figures 12–15 show the geometric factor of all bins to both protons and electrons. Table 5 summarizes the energy ranges measured by each Bin.

   Figure 12 shows the geometric factor of the Proton Bins 1–8 (Bins 6–13) as a function of proton energy. The threshold for proton detection is ~ 1.5 MeV which corresponds to the joint effect of the cutoff imposed by the beryllium window (~ 1.35 MeV), the threshold for detection (220 ± 20 keV), and noise in the first detector (14.64 keV). The energy range measured by each Proton Bin are well behaved with box-like structures and little overlap between each of them. Notice that Proton Bin 2 measures higher energies than Proton Bin 3. This is related to the fact that the Bin is attributed based on the deposited energy in the detector immediately before the one with the maximum deposited energy – in this case, detector #1. The algorithm assigns higher deposited energies to Proton Bin 3 which corresponds to lower proton energies according to the Bethe-Bloch formula. For the other Bins, this is no longer the case since no pair of Bins is assigned to the same detector (see Table 2). Also notice that there is a small dip in the geometric factor around 8 MeV for Proton Bin 3. This is due to these protons being assigned to Heavy Ion Bin 1 since they can deposit energies higher than the threshold for the algorithm to identify them as heavy ions. It is also noteworthy that for proton energies below ~ 20 MeV, the geometric factor matches the theoretical geometric factor. This is not the case for higher proton energies since the collimator starts to become transparent up to ~ 100 MeV where protons can reach the detectors after travelling through the whole collimator. Figure 13 shows the geometric factor of Electron Bins 1–5 (Bins 1–5) to as a function of proton energy. Only Electron Bin 2 was found to be significantly sensitive to low energy protons ~ 1.5–1.55 MeV. All Electron Bins are sensitive to high energy protons (> 100 MeV) since these can cross BERM's mechanical structure and deposit a relatively low energy in the detectors given that they are minimum ionizing particles.

   Figure 14 shows the geometric factor of the Electron Bins 1–5 (Bins 1–5) as a function of electron energy. The geometric factor never reaches the theoretical value since electrons are minimum ionizing particles, and the threshold is relatively high (220 ± 20 keV). Electron Bins 3–5 have integral shapes with threshold for detection at 0.5, 1.1, and 2.6 MeV respectively. Electron Bin 5 has very low sensitivity which is a result of both interaction cross-section and the relatively high trigger threshold. Electron Bins 1–2 have peak sensitivities at 0.17 MeV and 0.3 MeV respectively. Both correspond to electrons depositing energy only in the first detector. Electron Bin 1 has a lower sensitivity since it is assigned to the lowest deposited energies and therefore, is more susceptible to the high threshold. Proton
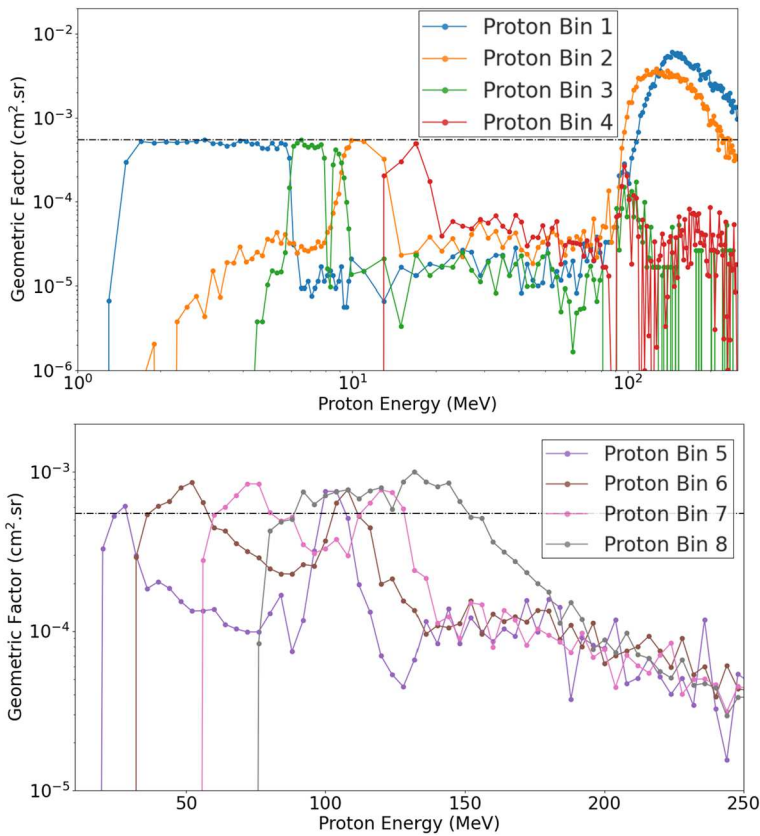
Fig. 12 Proton response functions of the Proton Bins 1–4 (top) and 5–8 (bottom). The black dashed line corresponds to the theoretical geometric factor calculated as per (Sullivan 1971). From 1.5 MeV to ∼ 95 MeV, the response functions of each bin are differential. For proton higher energies, protons can travel partially ($\geq$ 45 MeV) or through the whole collimator ($\geq$ 100 MeV). Consequently, at these energies, the total geometric factor surpasses the calculated value since the collimator no longer limits the field-of-view of the stack

Bin 1, 2, 4, 5 and 6 are sensitive to electrons with energies above ∼ 0.44, 0.33, 1.1, 1.3, and 6.5 MeV respectively, although with relatively low geometric factors.

It is worth noticing that the geometric factor for high protons energies (> 100 MeV) and all electrons are affected by the trigger threshold. For this reason, the Engineering Qualification Model (EQM), a replica of the flight model, will be tested with radioactive sources, and the flight measurements of BERM will be compared with other instruments aboard Bepi-Colombo, namely SIXS, to determine trigger threshold more accurately. The latter will also be used to validate the general shape of the response functions.

6 In-Flight Performance and First Results

Since the BepiColombo launch in October 2018, BERM has been measuring the interplanetary radiation environment. The background particle observations are in principle mainly composed of GCRs that are modulated by their interaction with the heliosphere. We expect
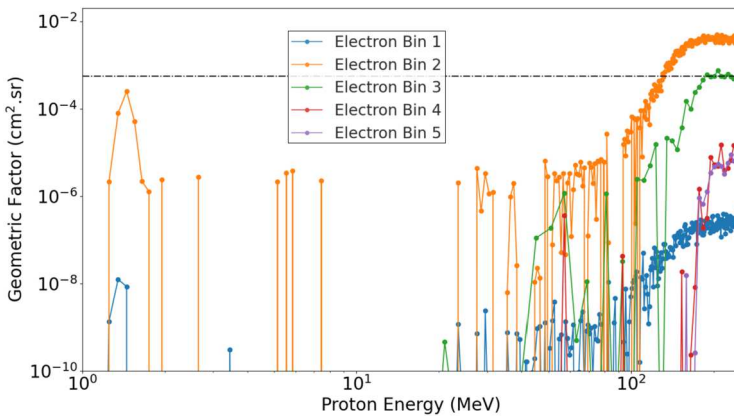
Fig. 13 Proton response functions of the Electron Bins 1–5 (Bins 1–5). The black dashed line corresponds to the theoretical geometric factor calculated as per (Sullivan 1971). Electron Bin 2 is sensitive to protons with energies between ~ 1.35–1.55 MeV and to protons with energies above 100 MeV. The other electron bins, more prominently Electron Bin 3, are sensitive to protons with energies above 100 MeV
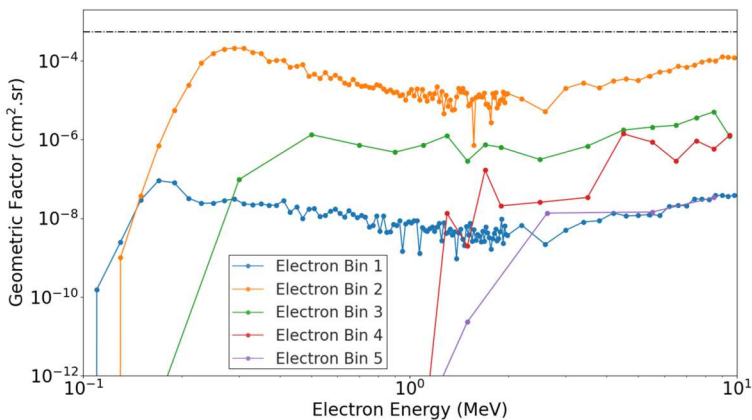

Fig. 14 Electron response functions of the Electron Bins 1–5 (Bins 1–5) from 0.1 to 10 MeV. The black dashed line corresponds to the theoretical geometric factor calculated as per (Sullivan 1971). Electron Bins 3–5 have integral geometric factors with an energy threshold for detections of ~ 0.5 MeV, ~ 1.1 MeV, and ~ 2.6 MeV respectively. Electron Bin 1 and 2 peak sensitivities are for electron energies of ~ 0.17 MeV and ~ 0.3 MeV respectively

that by the end of the cruise phase, in late 2025, BERM will provide accurate observations of GCR at the closest distances to the Sun, as well as their evolution with both the solar cycle and heliocentric distance, complementing previous studies made at farther distances (Honig et al. 2019; Roussos et al. 2020; Knutsen et al. 2021). Moreover, the background GCR flux can provide information of solar wind transients propagation, such as CMEs. When a CME crosses a point in space, a typical rapid reduction in the GCR flux is observed at that location, which is followed by a gradual recovery of several days. These reductions are called Forbush Decreases (FDs) and have been observed in the whole heliosphere (e.g. Witasse et al. 2017). At the time of writing, no large CMEs have occurred during the cruise due to the low solar activity levels, and so, it has not been possible to investigate the FDs so far. The
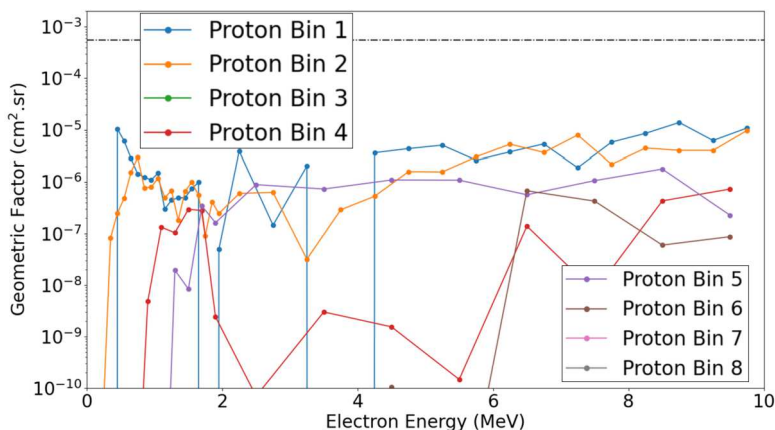
Fig. 15 Electron response functions of the Proton Bins 1–8 (Bins 6–13) from 0 to 10 MeV. The black dashed line corresponds to the theoretical geometric factor calculated as per (Sullivan 1971). Proton Bin 1, 2, 4, 5 and 6 are sensitive to electrons with energies above $\sim$ 0.44, 0.33, 1.1, 1.3, and 6.5 MeV respectively

Table 5 Bin detection energy range to electrons and protons. The sensitivity (geometric factor) varies between Bins. Most bins are sensitive to energies higher than shown here but with lower sensitivity

Bin	Electron energy (MeV)	Proton energy (MeV)
Electron Bin 1	0.17	100–∞
Electron Bin 2	0.3	1.35–1.55; 100–∞
Electron Bin 3	0.5–∞	100–∞
Electron Bin 4	1.1–∞	100–∞
Electron Bin 5	2.6–∞	100–∞
Proton Bin 1	0.44–∞	1.5–5.9; 103–∞
Proton Bin 2	0.33–∞	9.1–13; 103–∞
Proton Bin 3	NA	5.9–9.1
Proton Bin 4	1.1–∞	13–20.7
Proton Bin 5	1.3–∞	20.7–31.4; 95.6–109.2
Proton Bin 6	6.5–∞	31.4–59.1; 100–117
Proton Bin 7	NA	59.1–130
Proton Bin 8	NA	80.1–160

only exception has been during the BepiColombo Venus flyby 1, on 15 August 2020, where the Venus encounter coincided with a small CME-like solar transient and BERM showed a moderate decrease in the particle level at the same time of the CME-like arrival. After that, the measured particle flux was kept at a lower level during several days, which has been interpreted as a probable FD (Volwerk et al. 2021).

Thanks to the different planetary flybys that BepiColombo is performing, namely of Earth, Venus and Mercury (Mangano et al. 2021), we have the opportunity to test the capabilities of BERM prior to Mercury orbit insertion. This will allow to improve the instrument's calibration, cross-calibrate with other instruments, and measure the charged particles planetary fields. The measurements made by BERM during the flyby of Earth on 10 April 2020 are particularly useful. Figure 16 shows these observations. On the left panel, the geometry of the Earth flyby is presented. On the right panel, the BERM observations for the first three electron and proton bins are presented. As can be seen from both panels, Bepi-
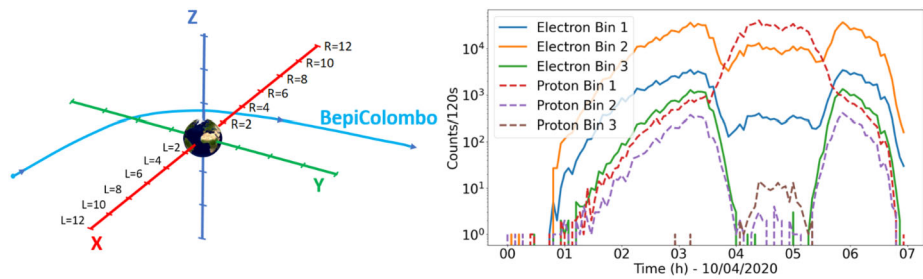
Fig. 16 (**a**) BepiColombo trajectory (in blue) during the Earth flyby on 10 April 2020 in Geocentric Solar Ecliptic (GSE) coordinates, where the X axis points towards the Sun, the Z axis is perpendicular to the plane of Earth orbit about the Sun (positive toward the North), and the Y axis completes the orthogonal system. (**b**) Radiation belt observations with BERM during the Earth flyby for Electron Bins 1–3 and Proton Bins 1–3

Colombo crossed the outer radiation belt at dawn, then skimmed the inner radiation belt, and finally crossed again the outer belt at night behind the dusk terminator. All presented bins except Proton Bin 3 measured the outer belt electrons. In general, this was expected since both Proton Bin 1 and Proton Bin 2 are sensitive to electrons while Proton Bin 3 is not. Proton Bin 1 and Electron Bin 3 have similar count rates in the outer belt. This is because their sensitivity to electrons ~ 0.5 MeV is very similar. Proton Bin 1 and 3 and Electron Bin 1 and 2 also show significant count rates in the inner belt. Proton Bin 2 shows negligible count rates in the inner belt mostly because it is sensitive to higher proton energies than Proton Bin 3 as shown in Fig. 12. The count rate of Electron Bin 1 is higher than expected. In fact, the expected count rate from the Geant4 simulations using the International Geostationary Electron model (IGE2006) (Sicard-Piet et al. 2008) is two orders of magnitude lower than what was measured, while the results for the other bins are within the same order of magnitude. This can be attributed to the unknown trigger value which may be lower than the one calculated for the calibration – Electron Bin 1 accounts for particles depositing an energy below ~ 0.15 MeV in the top detector. By lowering the trigger value from 0.215 MeV to 0.175 MeV, the Bin count rate increases by two orders of magnitude while the others remain close to the previous values. Triggers can still occur with threshold at 0.175 MeV because of the electronic noise, and because a Gaussian trigger is applied). This reinforces the necessity of performing additional tests to obtain the accurate value of the trigger threshold. The other Bins with significant count rates, Electron Bin 2, Electron Bin 3, Proton Bin 1, Proton Bin 2, and Proton Bin 3, show comparable results to the model.

Since the radiation belts were also observed by the SIXS instrument, a cross-calibration between SIXS and BERM is currently being performed. Calibration with respect to other terrestrial satellites such as the Cluster-II (Escoubet and Schmidt 2000), Themis (Angelopoulos 2008), and Arase/ERG missions (Matsuoka et al. 2018), will also be performed in a future publication. These joint observations are an important activity for cross-calibrations in preparation for the Hermean environment, and to validate BERM's characterization.

Regarding solar particles, the first observations of SEPs occurred during spring 2021 with the occurrence of several Solar flares accompanied by SEPs aligned with BepiColombo. Since SEPs are dependent on solar cycle activity, it is expected that more will occur later in the mission when higher levels of solar activity are reached. An example of a SEP detection by BERM in May 2021 is shown in Fig. 17, when BepiColombo was at 0.58 AU from the Sun. In this figure, the counts for a few bins have been summed over the period of 2 h with a moving window. A clear sharp enhancement is seen in Electron Bin 2 followed by a gradual reduction that lasts half of a day, and a small increase is seen at the end of day 9
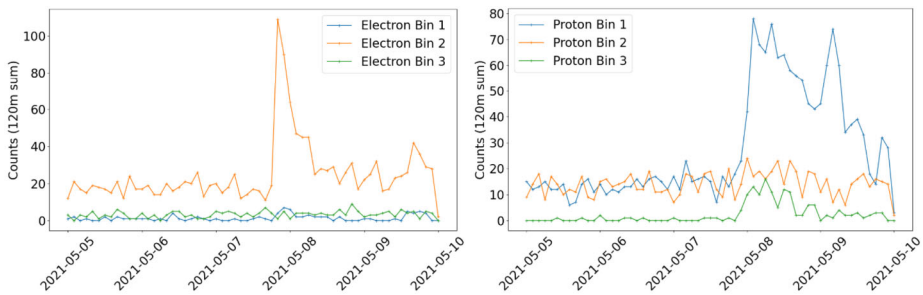
Fig. 17 BERM electron (left panel) and proton (right panel) detections during the solar energetic particle event that hit BepiColombo on 8 May 2021. The different colours indicate the measurements made by different BERM bins as indicated in the legend

before the instrument was switched off. The proton bins also see the SEP arrival, especially Proton Bin 1 although a bit later than in Electron Bin 2 as these particles are slower than electrons. There is also a sharp increase in protons at the beginning, but the recovery time is less gradual than for electrons, lasting at least 1.5 days (we note there is a gap of data at the end of the event). Electron Bin 2 is also sensitive to ~ 1.5 MeV protons so care must be taken when analysing its data. We also note that there is a second increase in Proton Bin 1 on day 9, which corresponds to the largest counts measured during this event in the proton channels and could be due to the passage of a coronal mass ejection as seen by other instruments in BepiColombo (not shown here).

The results presented here show the potential of BERM for characterizing both the Hermean and solar wind radiation environments, as well as its capability as sentinel to the other mission teams in case of potential damage to the spacecraft. It is expected that larger and more abundant solar events will be encountered during the cruise phase, as soon as the Sun reaches maximum activity in Solar cycle 25, which is expected near the time of orbit insertion at Mercury.

7 Conclusions

The BepiColombo Environment Radiation Monitor (BERM) was presented in this paper, including a full technical overview regarding its silicon stack detector, front-end electronics, and particle recognition algorithm. BERM is designed to detect energetic electrons, protons, and heavy ions in 18 particle/energy bins. Despite being a housekeeping instrument, BERM measurements will also provide valuable scientific information regarding the interplanetary and Hermean environment. Together with the scientific instruments of the BepiColombo mission such as SIXS, MGNS, MIXS, etc., BERM will study the Space Weather at Mercury including the effects of energetic particle on its magnetosphere, exosphere, and surface. It will also perform joint investigations of SEP and GCR propagation in the inner Solar System.

BERM ground calibration performed at PSI was revisited and used to study the instruments' behavior, and to create a Geant4 model of the detector capable of computing its proton and electron response functions. It was found that existing ground data is insufficient to characterize its trigger threshold. Tests using radioactive sources such as ^{90}Sr to characterize the trigger of BERM's Engineering Qualification Model are currently being planned. These tests will be critical to characterize the response to electrons and high energy protons.

We will also compare BERM's measurements during the Earth flyby to the SIXS' measurements in order to evaluate the response functions here presented.

We also showed measurements performed during the 10th of April 2020, Earth flyby, and a SEP event that hit BepiColombo on the 8th of May 2021. The results were obtained from six detection bins, the first three for electrons, and the first three for protons. Measurements made during the flyby were compared to the computed values using the response functions and a oeostationary electron model. It was demonstrated that bins that rely on low deposited energies on the first detector, namely Electron Bin 1, are extremely dependent on the trigger threshold reinforcing the importance of performing additional tests.

Overall BERM has been delivering promising results having shown its capability to measure electrons and protons, in SEPs and in the Earth's radiation belts. Nevertheless, more work is still required to comprehend the high energy bins corresponding to GCRs. The flexibility of BERM reconstruction algorithm allows it to be adapted to new findings. These include results from the on-going cross-calibration with other instruments such as SIXS that will be critical not only for future scientific investigation of the BepiColombo but also as a case-study for other missions carrying radiation monitors such as the JUpiter ICy moons Explorer scheduled for launch in 2023 (Grasset et al. 2013).

References

Agostinelli S et al (2003) Geant4 – a simulation toolkit. Nucl Instrum Methods A 506:250

Angelopoulos V (2008) The THEMIS mission. Space Sci Rev 141:5. https://doi.org/10.1007/s11214-008-9336-1

Arruda L et al (2017) SEP protons in GEO measured with the ESA multifunctional spectrometer. IEEE Trans Nucl Sci 64(8):2333–2339. https://doi.org/10.1109/TNS.2017.2714461

Baumjohann W, Matsuoka A, Narita Y et al (2020) The BepiColombo–Mio magnetometer en route to Mercury. Space Sci Rev 216:125. https://doi.org/10.1007/s11214-020-00754-y

Benkhoff J, Murakami G et al (2021) BepiColombo – mission overview and science goals. Planet Space Sci 217:90. https://doi.org/10.1007/s11214-021-00861-4

Bunce EJ, Martindale A, Lindsay S et al (2020) The BepiColombo Mercury Imaging X-Ray Spectrometer: science goals, instrument performance and operations. Space Sci Rev 216:126. https://doi.org/10.1007/s11214-020-00750-2

Escoubet CP, Schmidt R (2000) Cluster II: plasma measurements in three dimensions. Adv Space Res 25:1305

Forbush SE (1938) On world-wide changes in cosmic-ray intensity. Phys Rev 54:12,975–12,988

Fuente S et al (2016) BepiColombo MPO spacecraft pointing planning for science operations. In: SpaceOps 2016 Conference, AIAA 2016-2593

Grasset O et al (2013) JUpiter ICy moons Explorer (JUICE): an ESA mission to orbit Ganymede and to characterise the Jupiter system. Planet Space Sci 78:1

Heyner D, Auster HU, Fornaçon KH et al (2021) The BepiColombo planetary magnetometer MPO-MAG: what can we learn from the Hermean magnetic field? Space Sci Rev 217:52. https://doi.org/10.1007/s11214-021-00822-x

Honig T, Witasse OG, Evans H, Nieminen P, Kuulkers E, Taylor MGGT, Heber B, Guo J, Sánchez-Cano B (2019) Multi-point galactic cosmic ray measurements between 1 and 4.5 AU over a full solar cycle. Ann Geophys 37:903–918. https://doi.org/10.5194/angeo-37-903-2019

Huovelin J, Vainio R, Kilpua E et al (2020) Solar intensity X-ray and particle spectrometer SIXS: instrument design and first results. Space Sci Rev 216:94. https://doi.org/10.1007/s11214-020-00717-3

Jun I, Garrett HB, Evans RW (2019) Trapped particle environments of the outer planets. IEEE Trans Plasma Sci 47(8):3923–3930. https://doi.org/10.1109/TPS.2019.2907069

Knutsen EW, Witasse O, Sanchez-Cano B, Lester M, Wimmer-Schweingruber RF, Denis M, Godfrey J, Johnstone A (2021) Galactic cosmic ray modulation at Mars and beyond measured with EDACs on Mars Express and Rosetta. Astron Astrophys 650:A165. https://doi.org/10.1051/0004-6361/202140767

Mangano V, Dósa M, Fränz M et al (2021) BepiColombo science investigations during cruise and flybys at the Earth, Venus and Mercury. Space Sci Rev 217:23. https://doi.org/10.1007/s11214-021-00797-9

Matsuoka O, Teramoto R, Nomura R et al (2018) The ARASE (ERG) magnetic field investigation. Earth Planets Space 70:43. https://doi.org/10.1186/s40623-018-0800-1

Mitrofanov IG, Kozyrev AS, Lisov DI et al (2021) The Mercury Gamma-Ray and Neutron Spectrometer (MGNS) onboard the Mercury Planetary Orbiter of the BepiColombo mission: design updates and first measurements in space. Space Sci Rev 217:67. https://doi.org/10.1007/s11214-021-00842-7

Montagnon E, Budnik F, Casale M et al (2021) BepiColombo ground segment and mission operations. Space Sci Rev 217:32. https://doi.org/10.1007/s11214-021-00805-y

Murakami G, Hayakawa H, Ogawa H et al (2020) Mio – first comprehensive exploration of Mercury's space environment: mission overview. Space Sci Rev 216:113. https://doi.org/10.1007/s11214-020-00733-3

Orsini S et al (2021) SERENA: particle instrument suite for determining the Sun-Mercury interaction from BepiColombo. Space Sci Rev 217(1):11. https://doi.org/10.1007/s11214-020-00787-3

Pinto M, Gonçalves P (2019) GUIMesh: a tool to import STEP geometries into Geant4 via GDML. Comput Phys Commun 239:150–156. https://doi.org/10.1016/j.cpc.2019.01.024

Pinto M et al (2020) Beam test results of the RADEM Engineering Model. Nucl Instrum Methods Phys Res, Sect A, Accel Spectrom Detect Assoc Equip 958:162795. https://doi.org/10.1016/j.nima.2019.162795

Potgeiter MS, Burger RA, Ferreira SES (2001) Modulation of cosmic rays in the heliosphere from Solar minimum to maximum: a theoretical perspective. Space Sci Rev 97:295–307

Reames DV (1999) Particle acceleration at the Sun and in the heliosphere. Space Sci Rev 90:413–491. https://doi.org/10.1023/A:1005105831781

Roussos E, Dialynas K, Krupp N et al (2020) Long- and short-term variability of galactic cosmic-ray radial intensity gradients between 1 and 9.5 au: observations by Cassini, BESS, BESS-Polar, PAMELA, and AMS-02. Astrophys J 904:165. https://doi.org/10.3847/1538-4357/abc346

Saito Y, Delcourt D, Hirahara M et al (2021) Pre-flight calibration and near-Earth commissioning results of the Mercury Plasma Particle Experiment (MPPE) onboard MMO. Space Sci Rev 217:70. https://doi.org/10.1007/s11214-021-00839-2

Sicard-Piet A, Bourdarie S, Boscher D, Friedel RHW, Thomsen M, Goka T, Matsumoto H, Koshiishi H (2008) A new international geostationary electron model: IGE-2006, from 1 keV to 5.2 MeV. Space Weather 6(7):S07003. https://doi.org/10.1029/2007SW000368

Slavin JA, Baker DN, Gershman DJ, Ho GC, Imber SM, Krimigis SM, Sundberg T (2018) Mercury's dynamic magnetosphere. In: Solomon SC, Nittler LR, Anderson BJ (eds) Mercury: The View After MESSENGER. Cambridge University Press, Cambridge. Chap. 17

Sullivan JD (1971) Geometrical factor and directional response of single and multi-element particle telescopes. Nucl Instrum Methods I 95:5–11

Volwerk M, Sánchez-Cano B, Heyner D, Aizawa S, André N, Varsani A, Mieth J, Baumjohann W, Harrison R, Jeszenszky H, Fischer D, Futaana Y, Kazumasa I, Laky G, Miyoshi Y, Nakamura R, Plaschke F, Richter I, Rojas Mata S, Saito Y, Schmid D, Shiota D, Simon Wedlund C (2021) Venus's induced magnetosphere during active solar wind conditions at BepiColombo's Venus 1 flyby. Ann Geophys. https://doi.org/10.5194/angeo-2021-24

Witasse O et al (2017) Interplanetary coronal mass ejection observed at STEREO-A, Mars, comet 67P/Churyumov-Gerasimenko, Saturn, and New Horizons en route to Pluto: comparison of its Forbush decreases at 1.4, 3.1, and 9.9 AU. J Geophys Res Space Phys 122:7865–7890. https://doi.org/10.1002/2017JA023884